The Visible Absorption Spectrum of OBrO, Investigated by Fourier Transform Spectroscopy

Oliver C. Fleischmann,* Julian Meyer-Arnek, and John P. Burrows

Institute of Remote Sensing, University of Bremen, 28334 Bremen, Germany

Johannes Orphal

Laboratoire de Photophysique Moléculaire, Université de Paris-Sud, F-91405 Orsay Cedex, France

Received: November 6, 2004; In Final Form: March 13, 2005

By the utilization of a new laboratory method to synthesize OBrO employing an electric discharge, the visible absorption spectrum of gaseous OBrO has been investigated. Absorption spectra of OBrO have been recorded at 298 K, using a continuous-scan Fourier transform spectrometer at a spectral resolution of 0.8 cm^{-1}. A detailed vibrational and rotational analysis of the observed transitions has been carried out. The FTS measurements provide experimental evidence that the visible absorption spectrum of OBrO results from the electronic transition $C(^2A_2)-X(^2B_1)$. Vibrational constants have been determined for the $C(^2A_2)$ state ($\omega_1 = 648.3 \pm 1.9$ cm^{-1} and $\omega_2 = 212.8 \pm 1.2$ cm^{-1}) and for the $X(^2B_1)$ state ($\omega_1 = 804.1 \pm 0.8$ cm^{-1} and $\omega_2 = 312.2 \pm 0.5$ cm^{-1}). The vibrational bands (1,0,0), (2,0,0), and (1,1,0) show rotational structure, whereas the other observed bands are unstructured because of strong predissociation. Rotational constants have been determined experimentally for the upper electronic state $C(^2A_2)$. By modeling the band contours, predissociation lifetimes have been estimated. Further, an estimate for the absorption cross-section of OBrO has been made by assessing the bromine budget within the gas mixture, and atmospheric lifetimes of OBrO have been calculated using a photochemical model.

1. Introduction

The possible existence of OBrO in the lower polar stratosphere has been under discussion in recent atmospheric studies. On the basis of balloon-borne ultraviolet/visible (UV−vis) absorption measurements using the stellar occultation instrument Amon, Renard et al.[1] reported the first experimental evidence for the presence of OBrO during nighttime in the arctic stratosphere. The residual absorption features between 475 and 550 nm, recorded over Kiruna inside the polar vortex, were attributed to OBrO. The atmospheric concentration was estimated to be 10−20 pptv. Recently, Berthet et al.[2] analyzed observation data from the two balloon-borne absorption spectrometers Amon and Salomon.[3] The Salomon spectrometer uses lunar occultation. The data analysis by Berthet et al.[2] confirmed the observations made earlier by Renard et al.[1] The measurement accuracy was improved in part because of the new FTS absorption spectra of OBrO for the visible spectral range that were used in the data retrieval (O. Fleischmann, private communication). These FTS spectra are presented here in detail. The spectra were scaled by Berthet et al.[2] to absolute absorption cross-sections using a study by Knight et al.[4] Berthet et al.[2] observed a rise in the stratospheric OBrO concentration within the polar vortex at heights above 17 km up to 32 km. At altitudes between 25 and 32 km, the mixing ratio was estimated to be 5−15 pptv, while above 32 km, the concentration decreased again. The Salomon experiment showed further that, after dawn, the OBrO concentration diminished rapidly.

Other observations, however, yielded smaller concentrations for stratospheric OBrO. Erle et al.[5] estimated the typical nighttime concentrations in the stratosphere to 2.5 pptv, with a maximum value of 7.7 pptv. Some studies have tried to estimate the amount of atmospheric OBrO by chemical simulations. In a one-dimensional model based on gas-phase reactions only, Chipperfield et al.[6] estimated the likely concentration of OBrO to be less than 0.01 pptv.

The studies by Renard et al.[1] and Berthet et al.[2] indicated that remote sensing measurements in the visible range of atmospheric OBrO concentration are very sensitive to the wavelength calibration of the reference spectra employed. However, all previous recordings of the visible absorption spectrum of OBrO have relied on grating spectrographs.[4,7−9] Thus far, FTS that provides excellent wavelength calibration and stability has been applied to OBrO only in the mid-IR region.[10]

Although OClO had already been discovered in 1815 by Davy,[11] the gas-phase spectra of the two halogen dioxides OBrO and OIO were not observed until the 1990s by Rattigan et al.[7] and Himmelmann et al.,[12] respectively. Different spectroscopic studies of gaseous OBrO have been reported for the microwave, the IR, and the visible spectral range. The electronic ground state was investigated by Müller et al.[13] using microwave and by Chu et al.[10] using IR FTS. Müller et al.[13] analyzed the pure rotational spectrum, derived ground-state rotational and centrifugal distortion constants, and determined the ground-state molecular structure. Chu et al.[10] determined the fundamental vibrational frequencies of bands ν_1 and ν_3 for different isotopomers of OBrO. Miller et al.[9] scanned the visible absorption spectrum of OBrO using a monochromator and carried out a vibrational analysis. By comparing the experimental results to molecular constants derived from ab initio calculations, they

* Corresponding author. E-mail: oliver-cf@gmx.de.

10.1021/jp044911x CCC: $30.25
Published on Web 05/18/2005

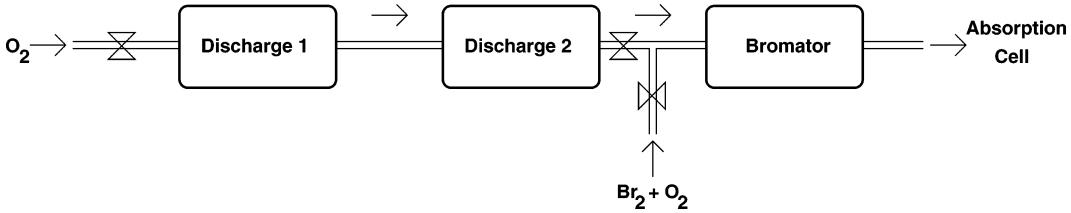

Figure 1. Experimental setup for the production of OBrO using a series of electric discharge chambers.

concluded that the visible absorption spectrum is due to the electronic transition $C(^2A_2)-X(^2B_1)$. Miller et al.[9] also calculated rotational constants for the excited electronic states and predicted that some rotational structure in the spectrum might be observable by high-resolution methods despite the predissociation broadening. This would enable the identification of the electronic state involved by a comparison of the rotational constants with those from ab initio predictions. Hence, this study anticipated one of the results presented here. The spectroscopic properties of OBrO have also been characterized in two ab initio studies by Peterson[14] and Vetter et al.[15] All these studies investigated the low-lying electronic states of OBrO that are relevant to the present study; Peterson[14] predicted vibrational and anharmonic, rotational, and centrifugal constants. Vetter et al.[15] further studied the potential energy surfaces and the possible dissociation channels of OBrO.

Here, we present FTS observations of the visible absorption spectrum of OBrO. A new method for the synthesis of OBrO by means of an electric discharge through mixtures of Br_2, O_3, and O_2 has been employed. This method yields a high OBrO concentration under flow conditions and has therefore enabled the recording of high-resolution FTS absorption spectra of OBrO in the visible spectral range. A vibrational and rotational analysis of the recorded absorption spectrum has been carried out. The spectroscopic analysis provides clear experimental evidence that the visible absorption spectrum of OBrO results from the electronic transition $C(^2A_2)-X(^2B_1)$, in agreement with theoretical predictions. The first experimental rotational constants and predissociation lifetimes for the excited electronic state $C(^2A_2)$ are reported. Further, an estimate for the absorption cross-section of OBrO in the visible spectral range is presented, and atmospheric lifetimes of OBrO have been calculated using a photochemical model.

2. Experimental Section

2.1. Synthesis of OBrO. OBrO was produced by a chain of electric discharge tubes, operating on a flow of O_2 and Br_2. The setup is drawn schematically in Figure 1. Three discharge chambers were connected in series. The first two discharges in flow direction were used to produce O_3 in a stream of O_2. The O_2 throughput was regulated to 500 standard $cm^3\ min^{-1}$(flow controller MKS 1259 CC). After passing the first two chambers, the oxygen flow had been enriched with 3−4% of ozone, which corresponded to an O_3 concentration of $(2-5) \times 10^{15}$ molecules/cm^3 in the absorption cell. The actual concentration of ozone depended on both pressure and flow throughput. The output of the second chamber was then connected to a third discharge tube. At the junction between the second and third discharge tubes, a small amount of Br_2 was added. Molecular oxygen served as the carrier gas for Br_2 with a flow rate of 10 standard $cm^3\ min^{-1}$. The stream into the third discharge chamber thus carried a gaseous mixture of O_2, O_3, and Br_2. This last discharge tube led to the production of OBrO. However, the mechanism of the formation of OBrO in the discharge is not quite clear yet.

The concentration of bromine was much smaller than that of ozone. With the third electric discharge turned off, the Br_2 concentration in the absorption cell was around $(2.5 \pm 0.8) \times 10^{13}$ molecules/cm^3. After turning on the last discharge, the cell concentration of Br_2 dropped to $(1.5 \pm 0.6) \times 10^{13}$ molecules/cm^3. Simultaneously, the spectral absorption features of OBrO appeared in the wavenumber region from 16 000 to 25 000 cm^{-1}. No change was observed in the O_3 concentration, as it was about 100× higher than for Br_2. As discussed below, the concentration of OBrO in the absorption cell was estimated to $(0.8-1.5) \times 10^{13}$ molecules cm^{-3}. The total cell pressure during the experiments was 50 ± 2 mbar.

In most of the previous laboratory studies, gaseous OBrO formation was initiated either by a photolysis or microwave discharge. Rattigan et al.[8] investigated the time-resolved photolysis of gas mixtures of Br_2 with a large excess of O_3. OBrO was observed as an intermediate species, and Rattigan et al.[8] assumed a formation of OBrO through the reaction $BrO + O_3 \rightarrow OBrO + O_2$. The estimated rate of this reaction indicated that it is probably of negligible significance for the chemistry of stratospheric ozone. Rowley et al.[16] also carried out photolysis experiments and stated that, for the laboratory production of OBrO, a minimum excess of O_3 over atomic Br of 10^4 was needed.

Several other experimental studies had relied on the dissociation of OBrO precursors by microwave-induced plasmas in a gas stream. Li[17] compared the efficiency for the OBrO formation by different gas mixtures that were led through a microwave discharge. The first mixture contained O_2 and He in the discharge. The atomic oxygen produced then reacted with Br_2. For the second method, Br_2 and He were brought into the discharge and later reacted with O_3. The highest production of OBrO was achieved by the third method, on the basis of a gas mixture of Br_2 and O_2 which was carried by He through the discharge. However, the concentration of OBrO obtained by microwave discharges was usually not sufficient for direct optical absorption measurements. Therefore, the sample initially had to be collected in a trap and later evaporated into the absorption cell. Other studies were based on similar production methods. Knight et al.[4] and Chu et al.[10] used the third of Li's[17] methods (Br_2/O_2/He), whereas Miller et al.[9] passed O_2 and He through the discharge.

For the recording of high-resolution FTS absorption spectra, an OBrO concentration of around 10^{13} molecules cm^{-3} was necessary in the absorption cell. Further, the experimental conditions had to remain unchanged over a period of at least 1 h. This favored a continuous-flow production similar to the established microwave discharge. The dissociation of precursors by an electric discharge appeared as an alternative. The earlier studies stimulated the idea of passing a mixture of Br_2 and excess O_3 through an electric discharge. The surplus of ozone corresponded to the observations made by Rattigan et al.[7] and Rowley et al.[16] This concept based on a series of electric discharge chambers proved to be successful, and an OBrO concentration of about $(0.8-1.5) \times 10^{13}$ molecules cm^{-3}

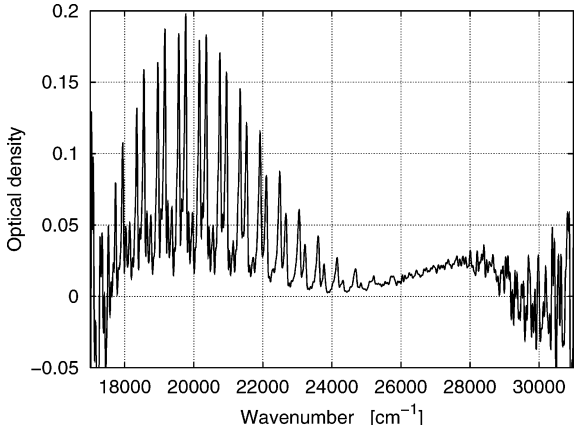

Figure 2. Optical density recorded when the electric discharges were turned on.

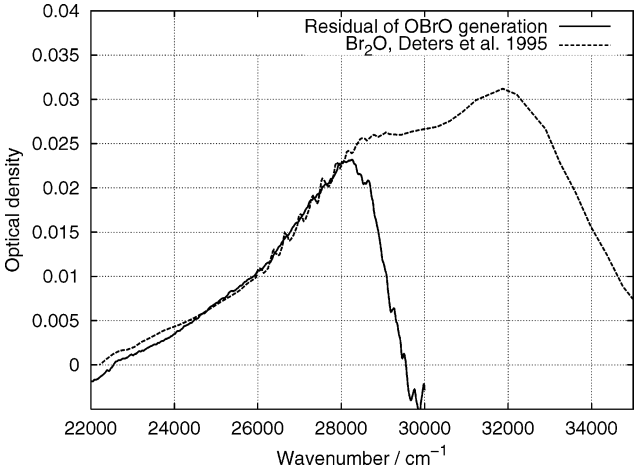

Figure 3. Unknown absorber component from the optical density plotted in Figure 2. The spectral resolution is 60 cm^{-1} fwhm. The reference shows the absorption spectrum of Br_2O, recorded in our laboratory and published by Deters et al.[19]

resulted under flow conditions. This is considerably higher than that achieved using microwave discharge of appropriate chemical mixtures in flow systems.

2.2. Absorption Spectrum of OBrO. The experimental setup to record the absorption spectra of OBrO comprised the gas source as described above, an absorption cell, and a continuous-scan FT spectrometer. Apart from the new gas source for OBrO, the setup has already been described elsewhere in detail.[18] Therefore, only a short summary is given here. The absorption cell had a length of 120 cm and consisted of three concentric glass jackets, the inner compartment (volume 3 1) being surrounded by a cooling mantle. On the outer side of the cooling compartment, an evacuated jacket isolated the inner chambers. The temperature of the inner cell carrying the probe gases was held constant at 298 K. The absorption chamber was operated under flow conditions, with a gas input at one end carrying O_3, O_2, Br_2, OBrO, and possibly other bromine oxides. The pump outlet was on the opposite end of the chamber. The cell pressure was kept at 50 ± 2 mbar. A high-pressure Xe lamp (Hamamatsu Super Quiet L2270) served as the analysis light source and was coupled into the gas chamber through quartz windows. The absorption path length in the gas chamber was extended by means of multipath White-type optics with aluminium mirrors that were coated with MgF_2. The mirrors were mounted internally to reduce losses caused by the cell windows. A total absorption path length of 1442 cm was established. After leaving the cell, the analysis light was coupled into a continuous-scan FT spectrometer (Bruker IFS 120 HR). A quartz beam splitter was employed, and a GaP photodiode was used as detector. Because the optical densities were below 0.3, high-resolution spectra of OBrO with a reasonable signal-to-noise ratio could only be recorded when limiting the bandwidth of the FTS. This was achieved by using electronic filters and changing the sampling intervals to record the range from 15 798 to 31 596.0 cm^{-1}. Absorption spectra were then recorded at a spectral resolution of 0.8 cm^{-1} fwhm.

In Figure 2, an absorption spectrum is plotted that was recorded with all discharge chambers switched on. For the background spectrum, the same cell content with discharges off was used. As Figure 2 indicates, the observable spectral range was reduced to wavenumbers below 30 000 cm^{-1}. First, this was caused by the mentioned bandwidth limitation of the FTS. Second, the UV light was absorbed strongly by the excess of ozone needed to produce OBrO. The reduced spectral width prohibited the observation of the UV−B and UV−C ranges. In particular, the UV absorption feature of OBrO above 33 000 cm^{-1} as observed by Knight et al.[4] could not be monitored by our measurement concept.

The maximum optical density of OBrO in the peak of the (6,1,0) band at 19 772 cm^{-1} was 0.2−0.3. When turning on the electric discharge, a part of the molecular bromine was disintegrated to form OBrO and other bromine oxides. This led to a negative optical density for Br_2, compared when the discharges were off. Figure 2 shows that the spectrum approaches zero in the region of Br_2 absorption around 24 000 cm^{-1}. The negative values for Br_2 are compensated by the positive optical density of OBrO. Significant amounts of BrO became visible only, when the concentration of Br_2 was increased above 4×10^{13} molecules/cm^3. Simultaneously, the concentration of OBrO decreased. For the recording of the FTS spectra, the experiments were optimized for a maximum yield of OBrO. In these measurements, no BrO features could be identified above the noise level.

Besides OBrO, O_3, and Br_2, a fourth absorption component appeared in the spectrum. Changes in the gas flow indicated that this component was independent from the other absorbers. However, the bandwidth limitation together with the large excess of ozone led to a very noisy spectrum above 29 000 cm^{-1}, and the optical densities were very small. This made the identification of the absorber difficult. In Figure 3, a smoothed spectrum (60 cm^{-1} fwhm) of the fourth absorber is plotted together with an absorption spectrum of Br_2O which had been recorded previously in our laboratory.[19] The characteristic of the unknown absorber that could be distinguished is the wavenumber position at 22 500 cm^{-1} where the spectrum begins to rise. On the basis of this feature, most of the other candidate species were ruled out, and Br_2O was tentatively attributed to this substance. The rather uncertain identification of the fourth absorber has little or no effect on the following spectroscopic analysis. Because this fourth component was clearly independent, it was separated from the OBrO spectrum. On the other hand, the estimation of the absorption cross-section of OBrO does depend on knowledge of this species.

After separating the different components of the optical density, an absorption spectrum for OBrO was obtained. The band system is plotted in Figure 4. Above the spectrum, vibrational quantum numbers are given to indicate the vibrational transitions. The spectrum obtained has been analyzed spectroscopically, and the results are discussed below. Additional measurements were carried out in order to estimate the

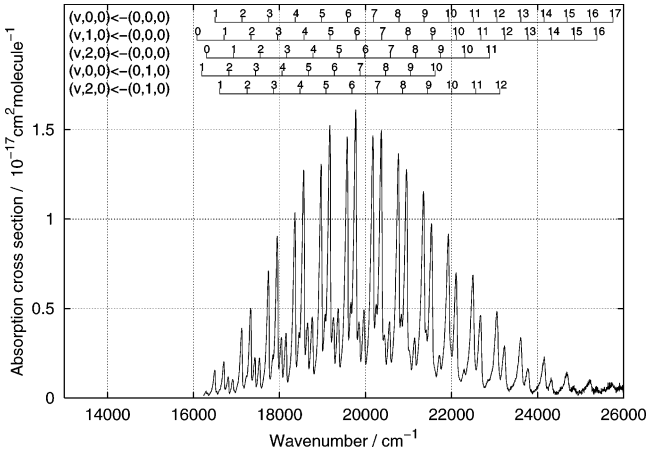

Figure 4. Absorption spectrum of OBrO. The markings above the spectrum indicate the vibrational quantum numbers for the different progressions involved.

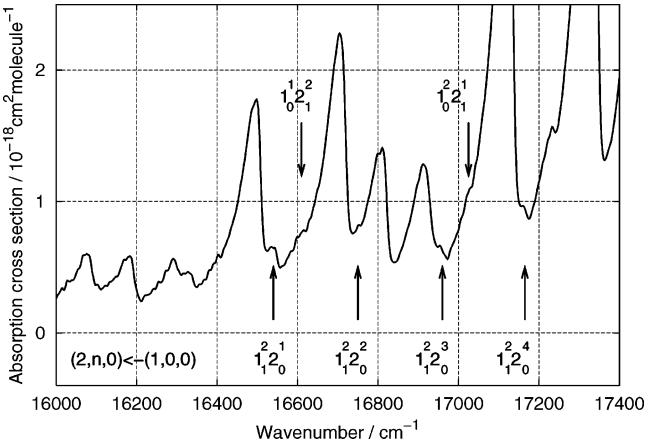

Figure 5. Newly observed vibrational bands in the visible absorption spectrum of OBrO. The arrows below the spectrum curve mark the bands that belong to the progression $(2,\nu_2',0)-(1,0,0)$. The labels indicate the ν_1 vibrational transitions by $1_{\nu''}^{\nu'}$ and the ν_2 transitions by $2_{\nu''}^{\nu'}$. The spectral resolution is 8 cm^{-1}.

absorption cross-section of OBrO. This was done by means of a bromine budget consideration, where different discharge states were established in the OBrO production chain. One or several discharge chambers were turned off, and the change of the absorption spectra in the gas compartment was observed. During these experiments, the input stream of the precursors O_2 and Br_2 remained unchanged. By considering the constant flow of Br_2 and the variation of optical densities caused by the electric discharges, the concentration of OBrO in the absorption cell was estimated to be $0.8-1.5 \times 10^{13}$ molecules cm^{-3}. The maximum amount of OBrO was obtained for a Br_2 concentration of $(2.5 \pm 0.8) \times 10^{13}$ molecules cm^{-3}.

3. Results and Discussion

On the basis of the recorded visible absorption spectrum of OBrO, the excited electronic state has been analyzed spectroscopically. By numerical simulations of the rovibronic bands, vibrational and rotational constants as well as predissociation line widths have been estimated. In the following, the vibrational results are discussed first. The rotational data that are presented provide clear experimental evidence that the visible absorption spectrum involves the upper electronic state $C(^2A_2)$. On the basis of the rotational constants, the structural parameters of OBrO have been derived. Further, the upper-state lifetimes have been estimated from the predissociation line widths.

3.1. Vibrational Analysis. The visible absorption spectrum of OBrO is formed by several vibrational progressions that accompany the electronic transition $C(^2A_2)-X(^2B_1)$. The vibrational quantum numbers were first assigned by Rattigan et al.[7] and later modified by Miller et al.,[9] after new bands had been observed. In Figure 4, the visible band system of OBrO, as recorded by the FTS measurements, is plotted. The upper-state progressions $(\nu_1',0,0)-(0,0,0)$ and $(\nu_1',1,0)-(0,0,0)$ from the vibrational ground state show the strongest absorption. Some progressions start from excited vibrational states, for example, the $(\nu_1',0,0)-(0,1,0)$ and $(\nu_1',2,0)-(0,1,0)$ series. The FTS absorption spectra further provide the first evidence for the progression $(2,\nu_2',0)-(1,0,0)$ up to $\nu_2' = 4$. The part of the spectrum where these bands are observed is shown in Figure 5. None of the bands in the visible absorption spectrum of OBrO could be assigned to transitions involving ν_3, which is in agreement with previous studies.

To determine the vibrational constants for the upper electronic state, the band origins in the visible spectrum had to be located first. This was achieved by a simulation of the rovibrational bands. Several bands were simulated, and the respective band origin was determined by shifting it on the wavenumber axis to obtain the best agreement with the experimental spectrum. The simulations and the results concerning rotational constants are discussed in the next section. The modeling of vibrational bands yielded the band origins $\tilde{\nu}_0$ and the rotational constants A, B, and C for most of the bands in the progressions $(\nu_1',0,0)-(0,0,0)$ and $(\nu_1',1,0)-(0,0,0)$. The origins of the observed bands are listed in Table 1, with progressions sorted into different columns. Most of the vibrational bands have already been observed by Miller et al.[9] The new bands first observed in this study, in particular, the progression $(2,\nu_2',0)-(1,0,0)$, are emphasized in the table. The wavenumber $\tilde{\nu}_0$ of a given band origin $(\nu_1',\nu_2',0)-(\nu_1'',\nu_2'',0)$ in the visible spectrum of OBrO can be described by the energy expression

$$\tilde{\nu}_0 = T_e + \omega_1'\left(\nu_1' + \frac{1}{2}\right) + \omega_2'\left(\nu_2' + \frac{1}{2}\right) + x_{11}'\left(\nu_1' + \frac{1}{2}\right)^2 + x_{22}'\left(\nu_2' + \frac{1}{2}\right)^2 + x_{12}'\left(\nu_1' + \frac{1}{2}\right)\left(\nu_2' + \frac{1}{2}\right) - \omega_1'\left(\nu_1'' + \frac{1}{2}\right) - \omega_2'\left(\nu_2'' + \frac{1}{2}\right)$$

$$\tilde{\nu}_0 = T_0 + (x_{11}' + x_{22}' + x_{12}')/4 + \left(\omega_1' + x_{11}' + \frac{x_{12}'}{2}\right)\nu_1' + \left(\omega_2' + x_{22}' + \frac{x_{12}'}{2}\right)\nu_2' + x_{11}'\nu_1'^2 + x_{22}'\nu_2'^2 + x_{12}'\nu_1'\nu_2' - \omega_1'\nu_1' - \omega_2''\nu_2'' \quad (1)$$

Here, T_e is the purely electronic energy difference between the upper and lower state. ω_1', ω_2', ω_1'', and ω_2'' are the vibrational constants for the upper and lower electronic states, and ν_1', ν_2', ν_1'', and ν_2'' are the respective vibrational quantum numbers. x_{11}' and x_{22}' are the first-order anharmonic constants in the upper state, and x_{12}' describes the coupling between ν_1' and ν_2' bands. No excitation of the ν_3 band was considered. Because the lower state's vibrations ω_1'' and ω_2'' were excited only up to one quantum at the temperature of 298 K, a determination of the anharmonic constants in the electronic ground state was not possible. T_0 is the energy of the transition $C(^2A_2)$ (0,0,0)$-X(^2B_1)$ (0,0,0). It is related to T_e by the expression $T_e = T_0 - E_0' + E_0''$, where $E_0 = (\omega_1 + \omega_2 + \omega_3)/2$ is the respective zero-point energy for the upper and lower electronic states.

TABLE 1: Band Origins (cm^{-1}) for the Observed Vibrational Bands in the Visible Absorption Spectrum of OBrO[a]

v′	(v_1',0,0)-(0,0,0)	(v_1',1,0)-(0,0,0)	(v_1',2,0)-(0,0,0)	(v_1',0,0)-(0,1,0)	(v_1'2,0)-(0,1,0)	(2,v_2',0)-(1,0,0)
0		16086	16305			16335
1	16504.4	16716	16927	16193	**16610**	**16542**
2	17133.1	17343	17549	16820	17246	**16750**
3	17755.0	17963	18167	17443	17862	**16960**
4	18372.5	18578	18780	18061	18475	**17165**
5	18983.1	19186	19386	18672	19080	
6	19589.1	19789	19985	19277	19684	
7	20188.8	20385	20579	19875	20275	
8	20783	20974	21166	20468	20862	
9	21370	21557	21744	21045	21437	
10	21949	22130	**22314**	**21620**	**22005**	
11	22521	22697	**22885**		**22565**	
12	23082	23256			**23122**	
13	23635	23803				
14	24180	24344				
15	24713	24878				
16	25245	25420				
17	25750					
18	**26240**					

[a] The bands are sorted into different progressions. The newly identified bands are in boldface type.

TABLE 2: Vibrational Constants (cm^{-1}) for the Electronic State C($^2A_2$)

parameter	T_e	T_0	ω_1	ω_2	ω_3	x_{11}	x_{22}	x_{12}
this work[a]	16190 ± 4	15861.5 ± 2.2	648.3 ± 1.9	212.8 ± 1.2		-3.55 ± 0.05	1.22 ± 0.05	-2.90 ± 0.15
this work[b]	16191 ± 4	15860.2 ± 2.2	643.3 ± 1.9	212.6 ± 1.2		-3.55 ± 0.05	1.22 ± 0.05	-2.90 ± 0.15
Miller et al.[9b,c]	≈16070	15863	641.5	210.7	(700)	−3.52	1.09	−2.70
Rattigan et al.[7c]	16178	16509	638	∼200	(700)	−3.58		
Kölm et al.[20d]		16785	631	221				
Peterson[14e,f]	16373		641.7	212.8	446.7	−2.54	−0.93	−2.45
Vetter et al.[15f]	16293							

[a] Vibrational energies are represented as $\tilde{\nu} = T_e + \omega_1'(\nu_1' + {}^1/_2) + x_{11}'(\nu_1' + {}^1/_2)^2 + \ldots$ [b] Vibrational energies are represented as $\tilde{\nu} = T_e + \omega_1'(\nu_1' + {}^1/_2) + x_{11}'\nu_1'^2 + \ldots$ [c] Rattigan et al.[7] and Miller et al.[9] estimated the value for ω_3. [d] Infrared argon matrix measurements using $O^{79}BrO$. [e] Isotopomer $O^{79}BrO$. [f] Ab initio study.

On the basis of the experimental band origins and eq 1, the vibrational constants were determined by a least-squares optimization. Because of the rising noise near the FTS bandwidth limitation, the (0,0,0) band was not observed. Therefore, the constant T_0 also had to be fitted. The results for the upper electronic state C($^2A_2$) are listed in Table 2. Values reported by earlier studies are also included. Miller et al.[9] used an expression slightly different from eq 1 to describe the vibrational energy terms: $\tilde{\nu}_0 = T_e + \omega_1'(\nu_1' + {}^1/_2) + \omega_2'(\nu_2' + {}^1/_2) + x_{11}'\nu_1'^2 + x_{22}'\nu_2'^2 + x_{12}'\nu_1'\nu_2'$. Because the half quanta for the anharmonic constants were not included, there was no linear dependence from x_{11}', x_{22}', x_{12}', in difference to eq 1. For a better comparison, the experimental FTS results for the vibrational constants are given in Table 2 for both definitions. The FTS results are generally in good agreement with the experimental values from Miller et al.[9] The results for ω_1' and ω_2' also harmonize with the theoretical predictions by Peterson.[14] For T_0, there are differences between the FTS results and the values by Rattigan et al.[7] and Kölm et al.[20] As Miller et al.[9] already pointed out, Rattigan et al.[7] had not observed the weak vibrational bands below 16 500 cm^{-1}. This led to an offset in the assignment of vibrational quantum numbers and hence to a different value for T_0. The value for ω_3' has not been determined by experiment so far, because no transition in the visible spectrum of OBrO could be assigned to it. The FTS results for the upper-state anharmonic constants x_{11}', x_{22}', and x_{12}' are similar to the experimental values reported by Miller et al.[9] and Rattigan et al.[7] Within the stated error intervals, the results for x_{11}' are identical. However, the ab initio study by Peterson[14] determined negative values for all three constants, which is the expected behavior for an anharmonic vibrational potential. On the other hand, both our study and the analysis by Miller et al.[9] yield a positive value for the second anharmonic constant x_{22}'. Richard and Vaida[21] reported a similar observation for OClO. They obtained a strongly positive value for the anharmonicity constant $x_{33}' = 13.15\ cm^{-1}$. It is assumed that this is caused by a Coriolis interaction between the symmetric ν_1' and the antisymmetric ν_3' bands of OClO. However, because the ν_2' vibration of OBrO is symmetric, the effect is not directly comparable.

TABLE 3: Vibrational Constants (cm^{-1}) for the Electronic State X($^2B_1$).

	ω_1	ω_2	ω_3
this work	804.1 ± 0.8	312.2 ± 0.5	
Miller et al.[19a]	799.4	317.5	848.6
Müller et al.[13b]	806.3	313.3	867.9
Kölm et al.[20c]	811.6	320.0	845.2
Miller et al.[9d]	797	317	845
Peterson[14d]	806.5	319.5	869.4

[a] Experimental results. [b] Force field calculations for $O^{79}BrO$, based on microwave rotational spectra. [c] Infrared argon matrix measurements using $O^{79}BrO$. [d] Ab initio study.

Table 3 summarizes the vibrational results for the electronic ground state X($^2B_1$). The vibrational frequencies have been determined using hot bands with vibrational excitation in the electronic ground state. The table compares the FTS values to previous studies based on different methods. The result of our study for ω_1'' is well within the range of earlier studies. The FTS result for ω_2'' is slightly smaller than the other references. Kölm et al.[20] performed IR measurements of OBrO in an argon matrix. Müller et al.[13] determined vibrational constants from force field calculations, on the basis of rotational microwave

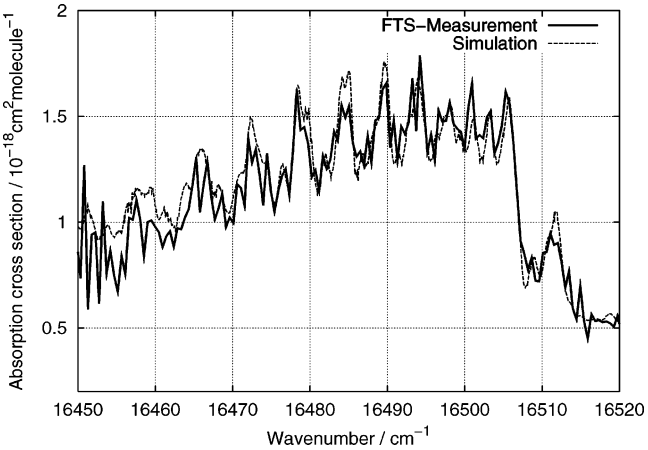

Figure 6. Comparison of experimental and simulated absorption spectrum for the rovibrational band (1,0,0)−(0,0,0). The spectral resolution was 0.8 cm^{-1} (fwhm) for the experimental spectrum and 0.15 cm^{-1} for the synthesized spectrum. For the simulated spectrum, a line width of 0.8 cm^{-1} (fwhm) was used.

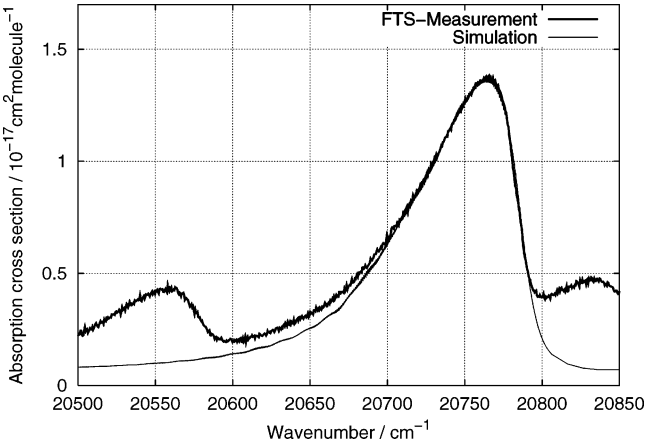

Figure 7. Comparison of experimental and simulated absorption spectrum for the rovibrational band (8,0,0)−(0,0,0). The spectral resolution was 0.8 cm^{-1} (fwhm) for the experimental spectrum and 0.15 cm^{-1} for the synthesized spectrum. For the simulated spectrum, a line width of 10 cm^{-1} (fwhm) was used.

spectra. The lower-state vibrational frequency ω_3'' could not be determined so far from observations in the visible spectral range. From IR FTS measurements, Miller et al.[9] obtained $\omega_3'' = 848.6$ cm^{-1}. The results from two ab initio investigations by Peterson[14] and Miller et al.[9] are also included in Table 3.

The pure electronic transition energy T_e was calculated from T_0 through $T_e = T_0 - E_0' + E_0''$. In the calculation, values for ω_1', ω_2'', ω_2', and ω_2'' were taken from the FTS measurements (see Tables 2 and 3). The experimental value $\omega_3'' = 848.6$ cm^{-1} as given by Miller et al.[9] and the ab initio value $\omega_3' = 446.7$ cm^{-1} as stated by Peterson[14] were used. This yielded $T_e = 16\,190 \pm 4$ cm^{-1}. Rattigan et al.[7] and Miller et al.[9] had estimated a value of 700 cm^{-1} for ω_3', which is bigger than ω_1'. An investigation of the inertial defect, as discussed below in the rotational analysis section, supports this relation between ω_3' and ω_1'. Using the approximation $\omega_3' \approx 700$ cm^{-1} to evaluate the FTS measurements, we obtained $T_e = 16\,063$ cm^{-1}. This result is close to the value $T_e = 16\,070$ cm^{-1}, which was derived by Miller et al.[9] with the same ω_3'. These similar results for T_e reflect the almost identical values for T_0 (see Table 2). The ab initio studies by Peterson[14] and Vetter et al.[15] obtained higher values for T_e than all experiments.

3.2. Rotational Analysis. While most of the vibrational bands in the visible absorption spectrum of OBrO are unstructured, rotational structure was observed in three bands. As an example, band (1,0,0) is plotted in Figure 6. The two other bands with rotational structure are the (2,0,0) and (1,1,0) bands. However, no individual lines could be distinguished, in contrast to microwave spectra.[13] Because OBrO is a rather heavy molecule of about 112 amu, the rotational lines are very densely grouped, with a few hundred lines per reciprocal centimeter (note that the full Doppler width in this spectral region is about 0.025 cm^{-1}). In addition, natural OBrO occurs in two main isotopic modifications, $O^{79}BrO$ and $O^{81}BrO$, with about equal natural abundances. Moreover, most lines are broadened because of predissociation. Altogether, this leads to a highly congested spectrum with no isolated lines. Because of the strong predissociation, however, an analysis of the predissociation lifetimes was possible and is presented below. For bands (3,0,0) and (4,0,0), the FTS observations suggest some residual rotational structure, but it could not be clearly separated from noise. For all other observed bands, no evidence for rotational structure was found at all. They are characterized by an unstructured smooth envelope, as shown for example in Figure 7.

Although most rotational lines in the visible absorption spectrum of OBrO are overlapping considerably, the principal rotational constants *A*, *B*, and *C* for the different bands were determined by analysis of the band contours. This was achieved through line-by-line simulations of the rovibrational bands. The transitions were calculated using a program for the asymmetric rotor written by Maki.[22] The constants *A*, *B*, and *C* for the electronic ground state $X(^2B_1)$ were taken from Müller et al.[13] Centrifugal distortion and higher-order constants or spin-rotation interaction terms were not included, because no individual rotational lines could be assigned. To achieve the best agreement between the synthesized and measured spectra, a least-squares optimization was carried out. The rotational constants *A*, *B*, and *C* for the upper electronic state and the band origins were varied until convergence was achieved. This was also applied to the smooth bands without rotational structure, where the individual band contours were modeled. A similar band contour analysis was carried out by Ashworth et al.[23] for OIO. The observed (1,0,0) band is plotted in Figure 6 together with the simulated spectrum. Figure 7 shows a second example with the unstructured (8,0,0) band.

OBrO is an asymmetric top molecule with three different moments of inertia. The asymmetry parameter $\kappa = (2B - A - C)/(A - C)$ for the electronic ground state $X(^2B_1)$ was determined experimentally by Müller et al.[13] as $\kappa = -0.823$. For the excited state $C(^2A_2)$, the FTS spectra yielded $\kappa = -0.622$. This is in agreement with theoretical predictions by Miller et al.[9] The rotational constants *B* and *C* are much smaller than *A* (Table 4). Because of the small value for κ, OBrO is a near prolate, only slightly asymmetric rotor.

The experimental rotational constants for the two upper-state progressions $(\nu_1',0,0)-(0,0,0)$ and $(\nu_1',1,0)-(0,0,0)$ are listed in Table 4. As shown in Figure 4, these two progressions dominate the electronic band system. The other bands are much weaker, which made it very difficult to determine the band shapes of the smaller bands. Rotational constants were therefore determined only for the two strongest progressions. The results for *A*, *B*, and *C* in the progression $(\nu_1',0,0)-(0,0,0)$ are also plotted in Figure 8 as a function of the vibrational quantum number ν_1. The error intervals (2σ) were determined by means of the least-squares optimization. The two isotopomers $O^{79}BrO$ and $O^{81}BrO$ could not be distinguished in the rotational analysis. The experimental uncertainties for the rotational constants were

TABLE 4: Rotational Constants *A*, *B*, and *C* in the Electronic State C($^2A_2$)[a]

	(ν'_1,0,0) ← (0,0,0)			(ν'_1,1,0) ← (0,0,0)		
ν'_1	A	B	C	A	B	C
1	0.623 ± 0.094	0.268 ± 0.048	0.183 ± 0.011	0.639 ± 0.117	0.266 ± 0.049	0.182 ± 0.012
2	0.618 ± 0.092	0.263 ± 0.016	0.180 ± 0.009	0.629 ± 0.092	0.265 ± 0.016	0.180 ± 0.010
3	0.624 ± 0.047	0.264 ± 0.007	0.182 ± 0.007	0.650 ± 0.074	0.269 ± 0.009	0.181 ± 0.008
4	0.582 ± 0.039	0.266 ± 0.006	0.178 ± 0.005	0.645 ± 0.068	0.267 ± 0.008	0.180 ± 0.010
5	0.612 ± 0.042	0.266 ± 0.008	0.176 ± 0.006	0.676 ± 0.072	0.268 ± 0.011	0.178 ± 0.011
6	0.594 ± 0.035	0.268 ± 0.006	0.172 ± 0.005	0.645 ± 0.067	0.270 ± 0.009	0.171 ± 0.009
7	0.612 ± 0.046	0.274 ± 0.008	0.157 ± 0.008	0.649 ± 0.089	0.268 ± 0.012	0.177 ± 0.012
8	0.542 ± 0.044	0.267 ± 0.008	0.169 ± 0.007	0.682 ± 0.063	0.271 ± 0.011	0.156 ± 0.011
9	0.589 ± 0.071	0.272 ± 0.014	0.136 ± 0.015	0.669 ± 0.085	0.273 ± 0.017	0.158 ± 0.020
10	0.579 ± 0.125	0.273 ± 0.025	0.130 ± 0.028	0.643 ± 0.139	0.277 ± 0.027	0.142 ± 0.026
11	0.516 ± 0.132	0.280 ± 0.027	0.121 ± 0.030	0.634 ± 0.155	0.275 ± 0.031	0.155 ± 0.026
12	0.555 ± 0.140	0.269 ± 0.036	0.138 ± 0.028	0.581 ± 0.182	0.269 ± 0.049	0.148 ± 0.034
13	0.538 ± 0.135	0.268 ± 0.038	0.145 ± 0.033	0.611 ± 0.171	0.270 ± 0.056	0.125 ± 0.041

[a]All values are given in reciprocal centimeters. The two progressions (ν'_1,0,0)−(0,0,0) and (ν'_1,1,0)−(0,0,0) of the electronic transition C($^2A_2$)−X($^2B_1$) were investigated. The error intervals represent a 2σ uncertainty.

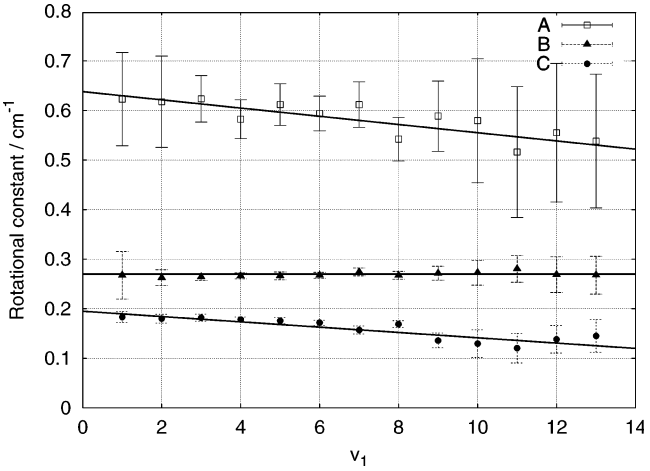

Figure 8. Rotational constants *A*, *B*, and *C* for the electronic state C($^2A_2$). The values for different rovibrational bands in the progression (ν_1,0,0)−(0,0,0) are plotted against the vibrational quantum number ν_1. The error bars represent a 2σ uncertainty.

between 5× and 100× bigger than the expected isotope splitting. Therefore, the stated results are valid for both isotopomers.

The rotational constants *A* and *C* decrease with higher excitation of the ν_1 vibration. This effect may be understood by the anharmonic electronic potential that leads to an increasing average internuclear distance and thus to smaller rotational constants. However, the effect is not observable for the constant *B*. Analytically, excitation of any vibrational mode ν_1, ν_2, and ν_3 or superpositions of them can cause a change in the three moments of inertia and hence a variation of the rotational constants *A*, *B*, and *C*. In a linear approximation, this is expressed by the constants α, as in the following expression

$$A_\nu = A_e - \alpha_1^A\left(\nu'_1 + \frac{1}{2}\right) - \alpha_2^A\left(\nu' + \frac{1}{2}\right) - \alpha_3^A\left(\nu'_3 + \frac{1}{2}\right) \quad (2)$$

Here, A_ν is the individual rotational constant for a given rovibrational band as listed in Table 4. A_e stands for the equilibrium rotational constant corresponding to the molecular geometry in the electronic potential minimum. For A_ν in the vibrational progression (ν'_1,0,0)−(0,0,0), it follows then

$$A_\nu = A_e - \alpha_1^A\left(\nu'_1 + \frac{1}{2}\right) - \frac{\alpha_2^A}{2} - \frac{\alpha_3^A}{2} \quad (3)$$

The constants α_1^A, α_1^B, and α_1^C are proportional to the slopes of the linear plots shown in Figure 8. They were derived from the FTS spectra using eq 3. The results are listed in Table 5. The error intervals represent twice the standard deviation (2σ) from the linear regression analysis. The parameters α_2^A, α_2^B, and α_2^C could not be properly derived, because only the strong bands for $\nu'_2 = 0$ and $\nu'_2 = 1$ were analyzed. The α_2 values exhibited error ranges of between ±130% and ±900%. Because no ν_3 transitions were observed, the constants α_3^A, α_3^B, and α_3^C could also not be determined. Therefore, the results for A_e, B_e, and C_e from this study still include contributions from α_2 and α_3, as, for example, for A_e

$$A_e \approx A_e - \frac{\alpha_2^A}{2} - \frac{\alpha_3^A}{2} = 0.639 \pm 0.026\ \mathrm{cm}^{-1}$$

However, as Table 5 shows, the constants α are about 100× smaller than the principal rotational constants *A*, *B*, and *C*. Therefore, A_e and other equilibrium values are expected to be the same as the $A_e - \alpha_2^A/2 - \alpha_3^A/2$ values within the error ranges of this study.

The most important result from the rotational analysis is the identification of the upper electronic state that causes the visible absorption spectrum of OBrO. Table 5 compares the FTS results for the upper-state rotational constants with the theoretical predictions by Miller et al.[9] and Peterson[14] for the lowest excited electronic states. Peterson[14] only characterized the C($^2A_2$) state so that no comparison between different excited states is possible. The experimental FTS results agree well with the predicted values by Peterson[14] for the electronic state C($^2A_2$). The FTS values are also close to the rotational constants predicted by Miller et al.[9] for the same electronic state. Further, they are quite different from the other electronic states A($^2B_2$) and B($^2A_1$). In summary, the rotational analysis of the FTS spectrum provides clear experimental evidence that the visible absorption spectrum is caused by the electronic transition C($^2A_2$)−X($^2B_1$).

From the rotational constants, the inertial defect $\Delta = I_C - I_A - I_B$ has been calculated. For a planar molecule like OBrO, a vanishing value is expected for the equilibrium structure, when no vibration is excited. This is confirmed by the experimental results. A value of $\Delta = -4.7 \pm 6.3$ amu Å^2 was obtained from the equilibrium rotational constants A_e, B_e, and C_e. The error interval for Δ reflects the uncertainties of the rotational constants from the linear regression (see Figure 8). To determine the inertial defect for the (0,0,0) vibrational band, which had not been observed, the rotational constants were derived indirectly from the equilibrium values by using eq 2. This yielded an

TABLE 5: Experimental Results and Ab Initio Values by Miller et al.[9] and Peterson[14] for the Rotational Constants in the Excited Electronic State[a]

param		this work (ν_1',0,0)−(0,0,0)	this work (ν_1',1,0)−(0,0,0)	ref 9 $A(^2B_2)$	ref 9 $B(^2A_1)$	ref 9 $C(^2A_2)$	ref 14 $C(^2A_2)$
A_e	[cm^{-1}]	0.639 ± 0.026	0.661 ± 0.032	0.4445	0.8907	0.6022	0.6270
B_e	[cm^{-1}]	0.264 ± 0.006	0.265 ± 0.004	0.3687	0.2272	0.2693	0.2661
C_e	[cm^{-1}]	0.197 ± 0.014	0.196 ± 0.010	0.2015	0.1810	0.1861	0.1868
α_1^A	[10^{-3} cm^{-1}]	7.5 ± 3.2	2.5 ± 3.8				1.08
α_1^B	[10^{-3} cm^{-1}]	−0.70 ± 0.60	−0.60 ± 0.38				1.78
α_1^C	[10^{-3} cm^{-1}]	5.0 ± 1.6	4.3 ± 1.2				0.954

[a] The error intervals represent 2× the standard deviation.

TABLE 6: Structural Parameters of OBrO for Several Electronic and Vibronic States[a]

electronic state	ref	A [cm^{-1}]	B [cm^{-1}]	C [cm^{-1}]	R [pm]	β [°]
$C(^2A_2)$	this work[b]	0.639 ± 0.026	0.264 ± 0.006	0.197 ± 0.014	176.9 ± 1.9	105.5 ± 1.3
$C(^2A_2)(1, 0, 0)$	this work	0.623 ± 0.094	0.268 ± 0.048	0.183 ± 0.011	176.8 ± 12.5	104.4 ± 6.6
$C(^2A_2)(10, 0, 0)$	this work	0.579 ± 0.125	0.273 ± 0.025	0.130 ± 0.028	178.4 ± 8.0	101.8 ± 6.1
$X(^2B_1)$	Miller et al.[9 c]	0.9268	0.2692	0.2086	166.0	114.8
$X(^2B_1)$	Müller et al.[13]	0.931	0.2746	0.2115	164.9	114.4
$A(^2B_2)$	Miller et al.[9 c]	0.4445	0.3687	0.2015	175.9	85.6
$B(^2A_1)$	Miller et al.[9 c]	0.8907	0.2272	0.1810	177.5	118.1
$C(^2A_2)$	Miller et al.[9 c]	0.6022	0.2693	0.1861	178.5	103.2
$C(^2A_2)$	Miller et al.[9 d]				175.9 ± 1.0	104.4 ± 0.5
$C(^2A_2)$	Peterson[14 c]	0.6270	0.2661	0.1868	177.8	104.64
$X(^2B_1)$	Vetter et al.[15 c]				165.2	114.5
$A(^2B_2)$	Vetter et al.[15 c]				174.9	86.1
$B(^2A_1)$	Vetter et al.[15 c]				176.8	117.3
$C(^2A_2)$	Vetter et al.[15c]				178.4	104.0

[a] The error intervals represent 2× the standard deviation. [b] Electronic equilibrium structure without vibrational excitation. [c] Ab initio study. [d] Franck−Condon analysis.

inertial defect $\Delta = -3.4 \pm 9.4$ amu Å^2, which is again equal to zero, within the error ranges.

With higher vibrational excitations in the ν_1 vibration, positive values were always observed for the inertial defect. For example, in the band (10,0,0), we obtained $\Delta = 38.8 \pm 8.1$ amu Å^2. Following the theory of Oka and Morino,[24] the positive inertial defect of OBrO with respect to excitation of the ν_1 vibration in the $C(^2A_2)$ state indicates that ω_3' is higher in energy than ω_1'. Further, the rather large value for Δ can be understood if the energy difference between these two vibrations is small. In this case, there should be a strong Coriolis interaction between the ν_1 and ν_3 vibrations in the excited electronic state $C(^2A_2)$. Future spectroscopic studies are required to solve this problem.

3.3. Structure of OBrO. From the rotational constants A and B, the Br−O bond length R and the bond angle β of OBrO were determined. In a first step, the principal moments of inertia were derived. Generally, rotational constant A (in cm^{-1}) is related to the respective moment of inertia I_A through $I_A = h/8\pi^2cA$, where c is the speed of light and h the Planck constant. The bond length and the bond angle were determined analytically from the moments of inertia I_A and I_B. In the analysis, the atoms were treated as point masses.

Table 6 summarizes the experimental results and compares them to other experimental and ab initio investigations. The FTS measurements for the excited electronic state, presumably the C-state, yielded an equilibrium bond length of $R = 176.9 \pm 1.9$ pm and a bond angle of $\beta = 105.5 \pm 1.3°$. These equilibrium structure parameters were derived from A_e, B_e, and C_e, which had been obtained from the linear regression analysis. The structure parameters for the individual bands (1,0,0) and (10,0,0) are also included in Table 6. They were determined using the rotational constants for each band, which caused larger error intervals.

Table 6 shows that the results for the structure parameters of OBrO are close to the theoretical predictions by Miller et al.,[9] Peterson,[14] and Vetter et al.[15] for the state $C(^2A_2)$. Within the uncertainties, the results for $C(^2A_2)$ are in agreement with the ab initio predictions. The bond length R has a rather small variation between the different electronic states, whereas the bond angle β changes significantly. The rotational constants from the FTS spectra also show a good agreement with the ab initio values reported by Peterson[14] (see Table 5). Because the structure parameters were derived from the rotational constants, agreement is observed again for the Br−O bond length and bond angle. Miller et al.[9] also carried out Franck−Condon simulations to find the best agreement between measured and theoretical absorption spectra. The Franck−Condon analysis yielded a bond length of $R = 175.9 \pm 1.0$ pm and a bond angle of $\beta = 104.4 \pm 0.5°$, which both agree with the values from the present study.

The FTS results for the rotational constants and structural parameters hence lead to a clear identification of the upper electronic state involved, on the basis of the earlier ab initio calculations, and confirm the conclusion by Miller et al.[9] that the visible absorption spectrum of OBrO is caused by the electronic transition $C(^2A_2)-X(^2B_1)$.

3.4. Predissociation. Most of the vibrational bands in the visible absorption spectrum of OBrO exhibit no rotational structure. The reason for this is a broadening of rotational lines and a resulting overlap. The rotational line widths were estimated by simulation of the rovibrational bands. The line width (fwhm) rises from 2 cm^{-1} for the (2,0,0) band to about 40 cm^{-1} for the (15,0,0) band (see Table 7). Hence, the line widths show a strong increase with vibrational excitation, and they are significantly larger than the instrumental resolution (0.8 cm^{-1}) or the Doppler width (0.025 cm^{-1}). Predissociation is therefore assumed to be the dominating broadening effect. A

TABLE 7: Rotational Line Width (fwhm) and Average Lifetime τ for the Upper States in the Progression (ν'_1,0,0)−(0,0,0)[a]

ν'_1		1	2	3	4	5	6	7
$\Delta\tilde{\nu}_{total}$	[cm^{-1}]	0.8	1.8−2.3	2.5−4	3−4.5	4−6	5−7	7−11
$\Delta\tilde{\nu}_{prediss}$	[cm^{-1}]	≤0.5	1.6−2.1	2.5−4	3−4.5	4−6	5−7	7−11
τ	[fs]	≥10^4	2500−3300	1330−2120	1180−1770	880−1330	760−1060	480−760

ν'_1		8	9	10	11	12	13	14	15
$\Delta\tilde{\nu}_{total}$	[cm^{-1}]	8−12	11−15	15−22	24−32	26−34	28−36	28−36	30−40
$\Delta\tilde{\nu}_{prediss}$	[cm^{-1}]	8−12	11−15	15−22	24−32	26−34	28−36	28−36	30−40
τ	[fs]	440−660	355−480	240−355	165−220	155−205	145−190	145−190	130−180

[a]The total line width $\Delta\tilde{\nu}_{total}$ has contributions from the instrumental line width (0.8 cm^{-1}) and the predissociation line width $\Delta\tilde{\nu}_{prediss}$.

similar behavior was found by Ashworth et al.[23] for OIO, and is also well-known for OClO.[25]

The assumption that the rotational lines are broadened by predissociation is also supported by ab initio calculations on OBrO by Vetter et al.[15] The three excited electronic states A($^2B_2$), B($^2A_1$), and C($^2A_2$) correlate with two dissociative limits, BrO + O and Br + O_2, and there are several pathways for OBrO to photodissociate. According to the calculations, a photon absorption at 2.5 eV (∼20 200 cm^{-1}) or higher energies most probably leads to the excitation of the C($^2A_2$) state, because the transition C($^2A_2$)−X($^2B_1$) has a much stronger transition dipole moment than the other single-electron transitions, A($^2B_2$)−X($^2B_1$) and B($^2A_1$)−X($^2B_1$). At photon energies above 2.8 eV (22 583 cm^{-1}), OBrO can dissociate directly from the C($^2A_2$) state to BrO + O. On the other hand, the energy barrier for the dissociation to Br + O_2 is lowest when the molecule is in the A($^2B_2$) state. Vetter et al.[15] further stated that in the energy range 2.4−2.7 eV (19 350−21 780 cm^{-1}) the three excited states are close to or crossing each other. This strongly increases the probability for radiationless transitions and limits the lifetime of the initial upper state after photon absorption. Eventually, OBrO may dissociate from any of the mentioned excited electronic states.

Lifetime broadening of absorption lines leads to a Lorentzian line shape with the full half-width $\Delta\tilde{\nu} = 1/(2\pi c\tau)$, where τ is the average lifetime of the excited state. To determine the lifetimes caused by predissociation, the simulated rotational bands were convoluted with a Lorentz function. The half-width was varied to yield the best agreement between simulated and theoretical spectrum. The results for different vibrational bands of the progression (ν'_1,0,0)−(0,0,0) are given in Table 7. The total line width $\Delta\tilde{\nu}_{total}$ includes the instrumental line width (0.8 cm^{-1}) and the predissociation line width $\Delta\tilde{\nu}_{prediss}$. The Doppler width (0.025 cm^{-1}) is comparably small and was therefore neglected. The results show that the average lifetime τ of OBrO due to predissociation from the state C($^2A_2$) decreases to 155 ± 25 fs for $\nu'_1 = 15$. Ashworth et al.[23] observed similar values for OIO (200 ± 50 fs). Hence, the predissociation of OBrO occurs much more rapidly than a fluorescence process, which happens after typically 10^{-6}−10^{-10} s. It may therefore be expected that the absorption of sunlight in the visible spectral range primarily leads to rapid photolysis of the molecule. We have assumed an efficency of 100% for the photodissociation by visible light and estimated the atmospheric photolysis rate of OBrO (see below).

For the (1,0,0) band, the total line width was smaller than the spectral resolution of 0.8 cm^{-1}, and the predissociation lifetime could not be determined well. For the (2,0,0) band, the total line width is around 2 cm^{-1}. For all higher vibrational excitations, the reduced lifetime dominates the line broadening. For $\nu'_1 \geq 8$, the rotational line width is of the same magnitude as the total width of the respective rotational−vibrational *band*. This leads to band envelopes being dominated by the Lorentz function. However, as Figure 7 shows, the asymmetry of the band shape, which is typical for a rovibrational band in an electronic transition, still remains. The asymmetric form is caused by large differences of the rotational constants between the lower and upper electronic states. As the Table 6 shows, the main rotational constants *A*, *B*, and *C* are smaller in the excited electronic state C($^2A_2$) compared to the ground state X($^2B_1$). This causes a degradation of the rovibrational bands to smaller wavenumbers. The bands are characterized by a broad rotational P-branch on the red side of the band origin and a narrow R-branch band head on the shortwave side. A similar behavior was observed by Ashworth et al.[23] for the OIO molecule.

3.5. Estimation of Absorption Cross-Section of OBrO. The absorption cross-section of OBrO has been estimated by utilizing the electric discharge synthesis. The analysis approach considers the bromine budget between the different bromine-containing species. It assumes that all bromine-containing compounds are observed and that the total amount of bromine is constant. This means that the part of the Br_2 from the input stream, which is dissociated by the electric discharge, is distributed among various bromine compounds by chemical reactions. These compounds comprise OBrO, Br_2O, and possibly a few higher oxides of bromine. The sum of all bromine-containing products equals the amount of Br_2 that has been removed by electric discharge and/or subsequent reaction.

Before switching on the electric discharges, the only bromine-containing compound that was observed in the absorption cell was Br_2. The discharge was then turned on without changing the input gas flow, and an absorption spectrum was recorded. As background, the previous spectrum with discharges off was used. The optical density now showed a decrease of Br_2, while bromine oxides appeared. Apart from Br_2 and O_3, the optical density spectra had contributions from OBrO and Br_2O. As discussed above, no further components could be identified above the noise level. In the concentration range used for Br_2, no BrO was present in the recorded spectra either. However, some earlier studies on OBrO and Br_2O have discussed the appearance of higher bromine oxides in gas mixtures of ozone and bromine.[4,8] Higher oxides of bromine usually have an unstructured absorption spectrum in the visible range, which makes them difficult to distinguish from the reference. The possible reactions involving higher oxides of bromine are currently not well-characterized.

Taking into account only the observed Br species, we can express the bromine budget as

$$-\Delta[Br_2] = \frac{1}{2}\Delta[OBrO] + \Delta[Br_2O] \qquad (4)$$

The left side of eq 4 contains the concentration difference of Br_2, which is removed after the electrical discharge has been turned on. The concentrations on the right side represent the

TABLE 8: Determination of the Absorption Cross-Section of OBrO[a]

exp	$\Delta[Br_2]$ [10^{12} molecules/cm^3]	$\Delta[Br_2O]$ [10^{12} molecules/cm^3]	Δ[OBrO] [10^{12} molecules/cm^3]	OD_{OBrO} at 19 772 cm^{-1}	σ_{OBrO} [10^{-17}cm^2/molecule]
1	-8.66 ± 1.39	2.08 ± 0.63	13.2 ± 3.1	0.250 ± 0.025	1.31 ± 0.33
2	-8.67 ± 1.39	3.12 ± 0.94	11.1 ± 3.4	0.210 ± 0.021	1.31 ± 0.42
3	-10.8 ± 1.73	2.43 ± 0.73	16.6 ± 3.8	0.250 ± 0.025	1.04 ± 0.26
4	-9.02 ± 1.44	3.81 ± 1.14	10.4 ± 3.7	0.205 ± 0.021	1.37 ± 0.51
5	-10.1 ± 1.62	4.51 ± 1.35	11.2 ± 4.2	0.260 ± 0.026	1.61 ± 0.62
6	-10.7 ± 1.71	4.16 ± 1.25	13.1 ± 4.2	0.273 ± 0.027	1.45 ± 0.49

[a]The concentration of OBrO was estimated by eq 5. The absorption cross-section is given for the peak absorption at 19 772 cm^{-1} (505.8 nm) for a spectral resolution of 38 cm^{-1}. The error intervals represent 2× the standard deviation.

TABLE 9: Experimental Absorption Cross-Section of OBrO for the Absorption Maximum in the (6,1,0) Band at 19 772 cm^{-1} (505.8 nm)[a]

$\Delta\tilde{\nu}$ (fwhm)	[cm^{-1}]	1	5	10	25	38
this work	[10^{-17}cm^2/molecule]	1.62 ± 0.40	1.61 ± 0.40	1.59 ± 0.40	1.49 ± 0.38	1.35 ± 0.34
Knight et al.[4]	[10^{-17}cm^2/molecule]				1.96 ± 0.56	

[a]The FTS values are given for different spectral resolutions $\Delta\tilde{\nu}$'s. The error intervals represent 2× the standard deviation.

amounts of OBrO and Br_2O that are produced in the system. Equation 4 is considered to hold for flow conditions, provided that the input stream of Br_2 remains unchanged when switching on the discharge. The concentration of OBrO is given by

$$\Delta[\mathrm{OBrO}] = 2 \times (-\Delta[\mathrm{Br_2}] - \Delta[\mathrm{Br_2O}]) \qquad (5)$$

The concentrations of Br_2 and Br_2O were derived from the measured optical densities OD using the relation $c = \mathrm{OD}/\sigma L$. Here, c stands for the concentration, σ the reference absorption cross-section, and L the absorption path length. The measurement uncertainty of the OD was estimated to be ±15% for Br_2 and Br_2O and ±10% for OBrO. The reference spectrum for Br_2 was recorded in separate FTS measurements, whereas the absorption cross-section of Br_2O had been determined by Deters et al.[19] The cross-section scaling of the reference spectra was accurate to ±6% for Br_2 and ±26% for Br_2O. The uncertainties for the optical density and the cross-section combined to give the total inaccuracy in the determination of $\Delta[Br_2]$ (±16%), $\Delta[Br_2O]$ (±30%), and hence Δ[OBrO] (±25−38%). All error intervals represent 2× the standard deviation. Next, with the knowledge of the concentration difference Δ[OBrO] from eq 5, the absorption cross-section of OBrO was derived from the optical density

$$\sigma_{\mathrm{OBrO}}(\tilde{\nu}) = \frac{\mathrm{OD}_{\mathrm{OBrO}}(\tilde{\nu})}{\Delta[\mathrm{OBrO}]L} \qquad (6)$$

The visible absorption cross-section of OBrO was determined from six sets of measurements. The concentrations of the different absorbers and the calculation of σ_{OBrO} are summarized in Table 8. The cross-section is given for the absorption maximum of the (6,1,0) band at 19 772 cm^{-1} (505.8 nm). The average absorption cross-section of OBrO at 19 772 cm^{-1} is $(1.35 \pm 0.34) \times 10^{-17}$ cm^2/molecule at a spectral resolution of 38 cm^{-1} and a 2σ uncertainty.

Using a high-resolution spectrum (0.8 cm^{-1}), we derived the corresponding cross-section values for different spectral resolutions. They are summarized in Table 9. The only earlier study by Knight et al.[4] is also included. Knight et al. reported the first estimation of the visible absorption cross-section of OBrO, based on a titration with NO. The value is about 30% higher than the FTS result. However, within the large uncertainty limits, the two measurements agree. Some earlier studies have tried to estimate the absorption cross-section of OBrO by using the analogy with OClO. Miller et al.[9] expected a peak cross-section of $(1.5 \pm 1.0) \times 10^{-17}$ cm^2 molecule^{-1} for the maximum of the (6,1,0) band of OBrO. As Table 9 shows, this estimation is confirmed by the experimental values.

The absorption cross-section of OBrO as derived here represents a lower limit. The reason is that we cannot entirely exclude other bromine oxides in addition to OBrO and Br_2O. If more bromine-containing species were present in significant amounts, then the absorption cross-section would be an underestimate, because the concentration of OBrO would be overestimated. One further issue is that the bromine oxides including OBrO tend to deposit on the walls of reactors, as has been observed in earlier studies.[8,9] This behavior would again reduce the amount of OBrO that could be actually observed and hence lead to a higher absorption cross-section.

3.6. Photolysis of OBrO. Using the results for the absorption cross-section of OBrO, we have estimated the photolysis frequency of OBrO in the atmosphere by solar radiation. The large line widths indicate that predissociation processes typically occur within a picosecond after the excitation. Hence, they are much faster than the relaxation by emission. For this reason, we have assumed a quantum yield of 100% for the calculation of the photolysis rate. This implies that every absorbed photon leads to dissociation of the OBrO molecule. For daytime, the calculations yield a typical stratospheric lifetime of 2−5 s, with a maximum of 10 s. For zenith angles larger than 85° and altitudes below 10 km, the lifetime exceeds 10 s. Consequently, for most atmospheric geometries, OBrO will be photolyzed very quickly by solar radiation. This confirms the observation by Berthet et al.[2] and Renard et al.,[1] who observed significant amounts of OBrO during the night only.

4. Conclusion

A new synthesis method for OBrO, based on an electric discharge in gaseous mixtures of Br_2 and O_2, has been discovered. The technique yields a concentration of 10^{13} molecules/cm^3 under flow conditions, which is considerably higher than what has been achieved previously using microwave discharges. The large concentration of OBrO enabled the recording of high-resolution FTS absorption spectra (0.8 cm^{-1}) in the visible spectral range. The spectra revealed rotational structure in three vibrational bands. By a spectroscopic analysis, vibrational and rotational constants were obtained for the excited electronic state. The analysis of the FTS measurements and a comparison to earlier ab initio calculations led to an unambiguous identification of the upper electronic state involved. The

observations provide experimental proof for the earlier assumptions that the visible absorption spectrum of OBrO is caused by the electronic transition $C(^2A_2)-X(^2B_1)$.

On the basis of the observed broadening of rotational lines, predissociation lifetimes for the electronic state $C(^2A_2)$ have been determined. Further, an estimation for the visible absorption cross-section of OBrO is given.

The identification of the electronic transition together with the measured predissociation lifetimes help to characterize the possible photochemical behavior of OBrO in the atmosphere. The total effect of solar radiation on OBrO is formed by the two steps of absorption and subsequent dissociation. The FTS results confirm that the OBrO molecule is in the $C(^2A_2)$ state after photon absorption. The observed predissociation lifetimes further indicate a rapid dissociation from the excited electronic state, typically within a picosecond. Here, we take into account the ab initio results by Vetter et al.,[15] stating that the electronic state $C(^2A_2)$ of OBrO most likely dissociates into BrO + O, whereas the other channel forming Br + O_2 is less important. Consequently, we expect as an overall effect that the absorption of sunlight by OBrO leads to the rapid production of BrO + O.

Acknowledgment. This work was accomplished with support from the University of Bremen and the German Space Agency (DLR/Bo. grant no. 50EP9207). We gratefully acknowledge partial funding by the EU project THALOZ and the objectives of IGBP-IGAC and WCRP-SPARC.

References and Notes

(1) Renard, J.-B.; Pirre, M.; Huguenin, D.; Robert, C. *J. Geophys. Res.* **1998**, *103*, 25383.

(2) Berthet, G.; Renard, J.-B.; Chartier, M.; Pirre, M.; Robert, C. *J. Geophys. Res.* **2003**, *108*, 4161.

(3) Renard, J.-B.; Chartier, M.; Robert, C.; Chalumeau, G.; Berthet, G.; Pirre, M.; Pommerreau, J.-P.; Goutail, F. *Appl. Opt.* **2000**, *39*, 386.

(4) Knight, G.; Ravishankara, A. R.; Burkholder, J. B. *J. Phys. Chem. A* **2000**, *104*, 11121.

(5) Erle, F.; Platt, U.; Pfeilsticker, K. *Geophys. Res. Lett.* **2000**, *27*, 2217.

(6) Chipperfield, M. P.; Glassup, T.; Pundt, I.; Rattigan, O. V. *Geophys. Res. Lett.* **1998**, *25*, 3575.

(7) Rattigan, O. V.; Jones, R. L.; Cox, R. A. *Chem. Phys. Lett.* **1994**, *230*, 121.

(8) Rattigan, O. V.; Cox, R. A.; Jones, R. L. *J. Chem. Soc., Faraday Trans.* **1995**, *91*, 4189.

(9) Miller, C. E.; Nickolaisen, S. L.; Francisco, J. S.; Sander, S. P. *J. Chem. Phys.* **1997**, *107*, 2300.

(10) Chu, L. T.; Li, Z. *Chem. Phys. Lett.* **2000**, *330*, 68.

(11) Davy, H. *Philos. Trans.* **1815**, *105*, 214.

(12) Himmelmann, S.; Orphal, J.; Bovensmann, H.; Richter, A.; Ladstätter-Weissenmayer, A.; Burrows, J. P. *Chem. Phys. Lett.* **1996**, *251*, 330.

(13) Müller, H. S. P.; Miller, C. E.; Cohen, E. A. *J. Chem. Phys.* **1997**, *107*, 8292.

(14) Peterson, K. A. *J. Chem. Phys.* **1998**, *109*, 8864.

(15) Vetter, R.; Ritschel, T.; Zülicke, L.; Peterson, K. A. *J. Phys. Chem. A* **2003**, *107*, 1405.

(16) Rowley, D. M.; Harwood, M. H.; Freshwater, R. A.; Jones, R. L. *J. Phys. Chem. A* **1996**, *100*, 3020.

(17) Li, Z. *J. Phys. Chem.* **1999**, *103*, 1206.

(18) Fleischmann, O. C.; Orphal, J.; Burrows, J. P. *J. Photochem. Photobiol., A* **2003**, *157*, 127.

(19) Deters, B.; Burrows, J. P.; Himmelmann, S.; Blindauer, C. *Ann. Geophys.* **1995**, *14*, 468.

(20) Kölm, J.; Engdahl, A.; Schrems, O.; Nelander, B. *Chem. Phys.* **1997**, *214*, 313.

(21) Richard, E. C.; Vaida, V. *J. Chem. Phys.* **1991**, *94*, 153.

(22) Maki, A. G. Personal communication, 1993.

(23) Ashworth, S. H.; Allan, B. J.; Plane, J. M. C. *Geophys. Res. Lett.* **2002**, *29*, 1026.

(24) Oka T.; Morino, Y. *J. Mol. Spectrosc.* **1961**, *6*, 472.

(25) Michielsen, S.; Merer, A. J.; Rice, S. A.; Novak, F. A.; Freed, K. F.; Hamada, Y. *J. Chem. Phys. A* **1981**, *74*, 3089.